Supporting Information

for

Single Particle Nanoplasmonic Sensing in Individual Nanofluidic Channels

Joachim Fritzsche[1], *David Albinsson*[1], *Michael Fritzsche, Tomasz J. Antosiewicz*[3], *Fredrik Westerlund*[2*] *and Christoph Langhammer*[1*]

[1]Department of Physics and [2]Department of Biology and Biological Engineering, Chalmers University of Technology, 41296 Göteborg, Sweden

[3]Centre of New Technologies, University of Warsaw, 02-097 Warsaw, Poland

*fredrik.westerlund@chamers.se; clangham@chalmers.se

1. Cross sectional SEM imaging

In order to record the cross sectional SEM images shown in Figure 1 in the main text, reference arrays (5 µm pitch) of isolated nanochannels were fabricated in parallel with the fluidic system on the same chips, containing densely packed (1 µm pitch) gold disks. Both reference nanochannels and enclosed gold disks were identical in size with the corresponding structures of the nanofluidic systems; however, the rows of gold disks in adjacent reference channels were shifted by 20 nm with respect to each other (see Figure S1.a). The imaged chip was pre-diced from the backside to a depth of 400 µm (see Figure S1.b) with a dicing saw (DAD3350 / Disco) using a hubbed nickel bonded blade of 30 µm thickness, and manually broken along the cut. Subsequently, 10 nm of carbon was deposited with electron-beam evaporation (HVC600, AVAC) on the sliced surface in order to prevent electric charging during SEM imaging (Supra 60 VP, Zeiss) at 15 kV acceleration voltage, 2 mm working distance, and 1500000-fold magnification.

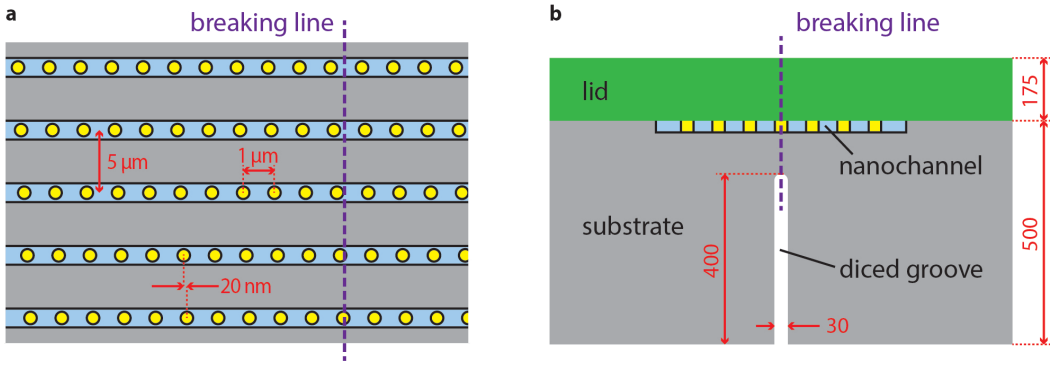

Figure S1 *Preparation of reference nanochannels for SEM imaging. (a) Top-view sketch, not to scale, of a reference array of nanochannels (blue) containing rows of evenly spaced gold nanoantennas. The small pitch between neighboring plasmonic sensors within each channel, together with the minute shift (20 nm) between adjacent rows of sensors, ensures that a straight perpendicular breaking line (purple) runs both through and close to some of the nanoantennas. (b) Cross-sectional schematics of the physical dimensions of the groove that allows for controlled cleaving of a chip perpendicular to the reference nanochannels (not true to scale). All dimensions are given in µm.*

2. Scattering spectra and bulk refractive index sensitivity of the nanotriangle

Figure S2 shows two scattering spectra of the triangular nanoantenna presented in Figure 1c for the cases of the hosting nanochannel being filled with water and with ethylene glycol (blue and red line, respectively). For this particular antenna, a bulk refractive index sensitivity of 138 nm follows from the shift of LSPR upon exchange of the two fluids of different refractive index, and the corresponding figure of merit (FoM) is 1.6. Note that the spectra were recorded in the same manner as those shown in Figure 1b, and that the y-axes of the two figures are identical.

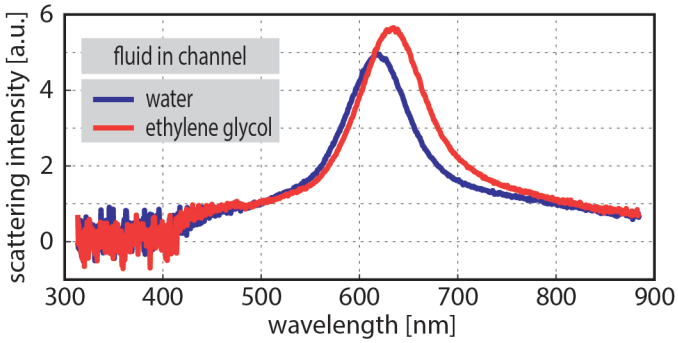

Figure S2. *Scattering spectra of the triangular nanoantenna presented in Figure 1c for the hosting nanochannel filled with water (blue line) and with ethylene glycol (red line).*

3. Fabrication of nanofluidic systems

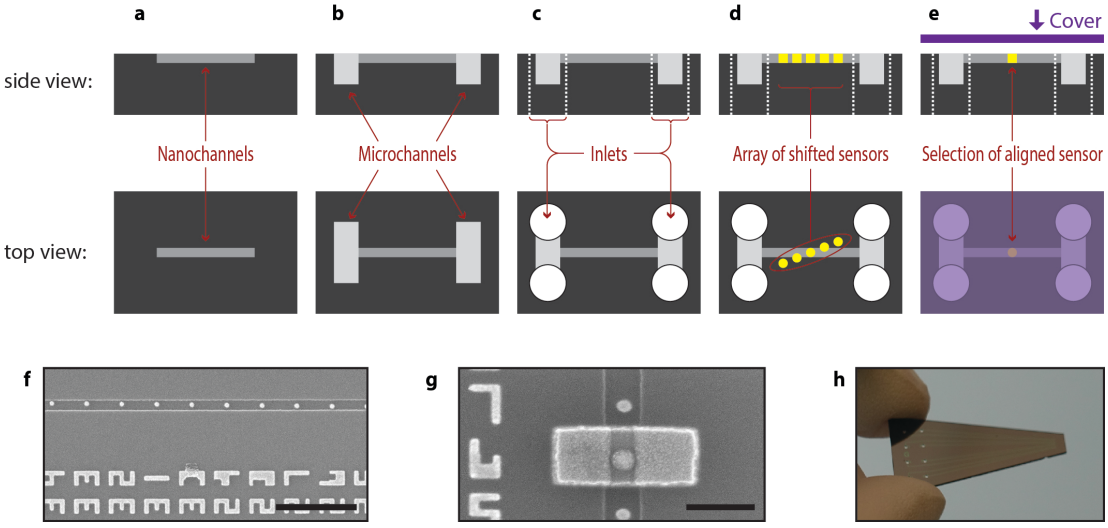

Figure S3. *Summary and schematic depictions of key nanofabrication steps: (a) Definition and etching of nanochannels with electron beam lithography and reactive-ion etching, respectively. (b) Etching of microchannels connecting to the nanochannels with optical lithography and reactive-ion etching. (c) Etching of inlet holes with photolithography and deep reactive-ion etching. (d) Definition of plasmonic nanoantenna sensors with electron beam lithography, and growth of the antennas via physical vapor deposition through the electron beam lithography mask, followed by lift-off. (e) Selection of well-aligned antennas, fusion bonding of the nanostructured Si-wafer to a glass cover wafer. (f) SEM image (3µm scale bar) of an array of antennas systematically shifted across a nanochannel corresponding to the schematics shown in (d). (g) SEM image (1µm scale-bar) of the particular antenna of an array that is best aligned with a nanochannel. An aluminum layer coating the chosen antenna enables selective removal of all other antennas with wet etching. (h) Photograph of the finalized nanofluidic device with integrated single particle plasmonic sensing capability.*

Fabrication of the nanofluidic systems was carried out in cleanroom facilities of Fed. Std.209 E Class 10 – 100, using electron-beam lithography (JBX-9300FS / JEOL Ltd), photolithography (MA 6 / Suss MicroTec), reactive-ion etching (Plasmalab 100 ICP180 / Oxford Plasma Technology), electron-beam evaporation (PVD 225 / Lesker), magnetron sputtering (MS150 / FHR), deep reactive-ion etching (STS ICP / STS) and wet oxidation (wet oxidation / Centrotherm), fusion bonding (AWF 12/65 / Lenton), and dicing (DAD3350 / Disco). In particular, the fabrication comprised the following processing steps of a 4”-silicon (p-type) wafer:

Reactive-ion etching of alignment marks – (a) Spin coating HMDS adhesion promoter (MicroChem) at 3000 rpm for 30 sec and soft baking on a hotplate (HP) at 115˚C for 120 sec. Spin coating UV5 (MicroChem) at 3000 rpm for 60 sec and soft baking (HP) at 130˚C for 120 sec. (b) Electron-beam exposure of alignment marks for both optical and electron-beam lithography at 10 nA with a shot pitch of 24 nm and 25 µC/cm2 exposure

dose. (c) Post-exposure bake (HP) at 130˚C for 90 sec. (d) Development in MF-24A (Microposit) for 90 sec, rinsing in water and drying under N2-stream. (e) Reactive-ion etching (RIE) for 15 sec at 60 mTorr chamber pressure, 60 W RF-power, 60 sccm O2-flow (descum). RIE for 30 min at 40 mTorr chamber pressure, 50 W RF-power, 100 W ICP-power, 50 sccm Cl2-flow (1200 nm etch depth in silicon).

Thermal oxidation: (a) Cleaning in 50 mL H2O2 + 100 mL H2SO4 at 130˚C for 10 min, rinsing in water and drying under N2-stream. (b) Wet oxidation in water atmosphere for 100 min at 1050˚C (110 nm thermal oxide).

Reactive-ion etching of nanochannels: (a) Electron-beam evaporation of 20 nm Cr (hard mask). (b) Spin coating ZEP520A : anisole (2:1) (ZEONREX Electronic Chemicals) at 2000 rpm for 60 sec and soft baking (HP) at 180˚C for 10 min. (c) Electron-beam exposure of lines at 2 nA with a shot pitch of 4 nm and 280 μC/cm2 exposure dose. (d) Development in n-amyl acetate for 120 sec, rinsing in isopropanol and drying under N2-stream. Covering alignment marks with Kapton tape. (e) RIE for 10 sec at 40 mTorr chamber pressure, 40 W RF-power, 40 sccm O2-flow (descum). RIE for 90 sec at 20 mTorr chamber pressure, 50 W RF-power, 200 W ICP-power, 20 sccm O2-flow, 50 sccm Cl2-flow (selective Cr hard-mask etch). RIE for 30 sec at 8 mTorr chamber pressure, 50 W RF-power, 50 sccm NF3-flow (30 nm etch depth in thermal oxide).

Etching of microchannels: (a) Spin coating HMDS at 3000 rpm for 30 sec and soft baking (HP) at 115˚C for 2 min. Spin coating S1813 (Shipley) at 3000 rpm for 30 sec and soft baking (HP) at 115˚C for 2 min. (b) Expose microchannels for 8 sec in contact aligner at 6 mW/cm2 intensity. (c) Development in MF-319 (Microposit) for 60 sec, rinsing in water and drying under N2-stream. (d) Buffered oxide-etch for 2 min to remove thermal oxide, rinsing in water and drying under N2-stream. (e) RIE for 30 min at 40 mTorr chamber pressure, 50 W RF-power, 100 W ICP-power, 50 sccm Cl2-flow (1200 nm etch depth in silicon). (f) Removal of resist in S1165 (Microposit) at 75˚C, rinsing in water and drying under N2-stream.

Deep reactive-ion etching of inlets: (a) Magnetron-sputtering of 200 nm Al (hard mask). (b) Spin coating S1813 at 3000 rpm for 30 sec and soft baking (HP) at 115˚C for 2 min. (c) Expose inlets for 10 sec in contact aligner at 6 mW/cm2 intensity. (d) Development in MF-319 for 60 sec, rinsing in water and drying under N2-stream. (e) Aluminum wet etch (H3PO4:CH3COOH:HNO3:H2O (4:4:1:1)) for 10 min to clear the hard mask at inlet positions. (f) Deep reactive-ion etching (SF6 / C4F8 based Bosch process) of inlets through the substrate. (g) Removal of Al-hard mask in aluminum wet etch (see above) for 60 min.

Fabrication of gold disk nanoantennas in the nanochannel: (a) Spin coating Copolymer MMA(8.5)MMA (MicroChem Corporation, 4 wt % diluted in anisole) at 3000 rpm for 60 sec and soft baking (HP) at 180˚C for 10 min. Spin coating ZEP520A : anisole (1:2) at 3000 rpm for 60 sec and soft baking (HP) at 180˚C for 10 min. (b) Electron-beam exposure of disks with 36 points at 1 nA with a shot pitch of 2 nm and 280 μC/cm2 exposure dose. (c) Development in n-amyl acetate for 120 sec, rinsing in isopropanol and drying under N2-stream. Development in methyl isobutyl ketone:isopropanol (1:1) for 120 sec, rinsing in isopropanol and drying under N2-stream. (d) Electron-beam evaporation of 30 nm Au. (e) Lift-off in acetone, rinsing in isopropanol, and drying under N2-stream.

Selection of well-aligned antennas: (a) SEM inspection of the wafer to identify those nanoantennas best aligned with the nanochannels. (b) Spin coating Copolymer MMA(8.5)MMA (MicroChem Corporation, 4 wt % diluted in anisole) at 1500 rpm for 60 sec and soft baking (HP) at 180˚C for 10 min. Spin coating ZEP520A : anisole (1:2) at 3000 rpm for 60 sec and soft baking (HP) at 180˚C for 10 min. (c) Electron-beam exposure of rectangular openings around the selected nanoantennas at 1 nA with a shot pitch of 2 nm and 280 μC/cm2 exposure dose. (d) Development in n-amyl acetate for 120 sec, rinsing in isopropanol and drying under N2-stream. Development in methyl isobutyl ketone:isopropanol (1:1) for 180 sec, rinsing in isopropanol and drying under N2-stream. (e) Electron-beam evaporation of 100 nm Al. (f) Lift-off in acetone, rinsing in isopropanol, and drying under N2-stream. (g) Removal of all not selected nanoantennas in Au wet-etch. (h) Removal of Al protection pads in MF-319 (Microposit) for 5 min.

Fusion bonding: (a) Cleaning of the substrate together with a lid (175 μm thick 4”-pyrex, UniversityWafers) in H2O:H2O2:HCl (5:1:1) for 10 min at 80˚C, and in H2O:H2O2:NH3OH (5:1:1) for 10 min at 80˚C. (b) Pre-bonding the lid to the substrate by bringing surfaces together and manually applying pressure. (c) Fusion bonding of the lid to the substrate for 5 h in N2 atmosphere at 550˚C (5˚C/min ramp rate).

Dicing: Cutting nanofluidic chips from the bonded wafer using a resin bonded diamond blade of 250 μm thickness (Dicing Blade Technology) at 35 krpm and 1 mm/s feed rate.

4. Suppression of light scattering from nanochannel walls

Light scattering from the channel walls is a concern because it interferes with the scattering from the nanoantenna in the channel and it also contributes to a high and unwanted background. Therefore it has to be suppressed. The effect of light scattered from the walls of water-filled channels with different widths (Figure S4a) upon illumination with unpolarized white light through a 50x dark field objective is illustrated in Figure S4b. Clearly the wall scattering decreases with decreasing channel width but is significant also for the narrowest (140 nm) channel.

To minimize this effect we present two different solutions. The first one relies on using the microscope's white light source and illumination through a dark-field objective in combination with a linear aperture (8 mm wide) aligned parallel to the nanochannel direction, and inserted between the microscope objective and the sample (Figure S4c). The second alternative is to use laser illumination at a shallow angle of incidence (i.e. not through the objective) along the channel direction (Figure S4d). The monochromatic illumination approach facilitates simultaneous readout of multiple nanochannels. A further advantage of monochromatic illumination sensing over traditional tracking of LSPR peak position is the redundancy of spectral resolution. This allows for simpler setups and more efficient use of detector surface since principally, for reading off a single nanoantenna signal, only one detector pixel is needed. It is also an attractive alternative to hyperspectral imaging, since it allows for faster data acquisition.

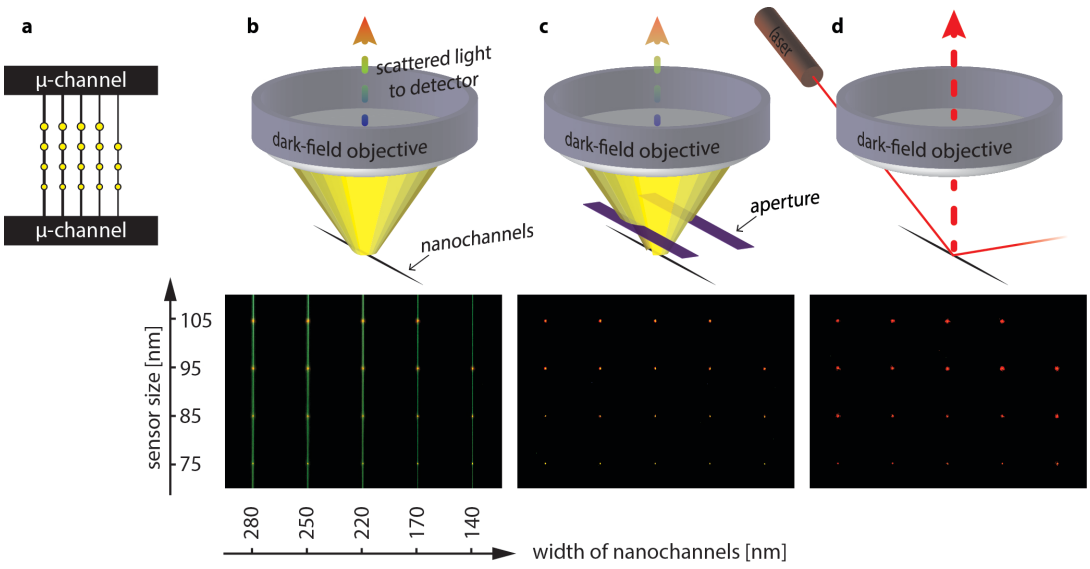

Figure S4. *Illumination schemes for minimizing light scattering from the nanochannel walls. (a) Schematic depiction of the device used for the investigation of the wall-scattering effect, featuring an array of nanochannels with different widths (280, 250, 220, 170 and*

140 nm) and constant depth of 25 nm, each integrated with Au nanodisks of the sizes 105, 95, 85 and 75 nm. Note that the largest particle in the narrowest channel intentionally is missing since it would almost block the channel. (b-d) Schematic depictions of the three different illumination schemes used (top), together with the corresponding dark-field microscopy image (bottom) of the device with water-filled nanochannels. The wall scattering effect is more prominent for wider nanochannels and can be suppressed efficiently by (c) using polychromatic (unpolarized halogen lamp) or (d) monochromatic (633 nm HeNe laser) illumination in the direction of the nanochannels, compared to the standard polychromatic illumination through the dark-field objective (b).

5. Raw data (spectra) corresponding to Figure 2

Figure S5 shows one raw data single particle scattering spectrum corresponding to each data point displayed in Figure 2b. Note that the data points in Figure 2b show the mean value derived from four spectra measured in sequence for every particle by every time refocusing the microscope prior to the measurement.

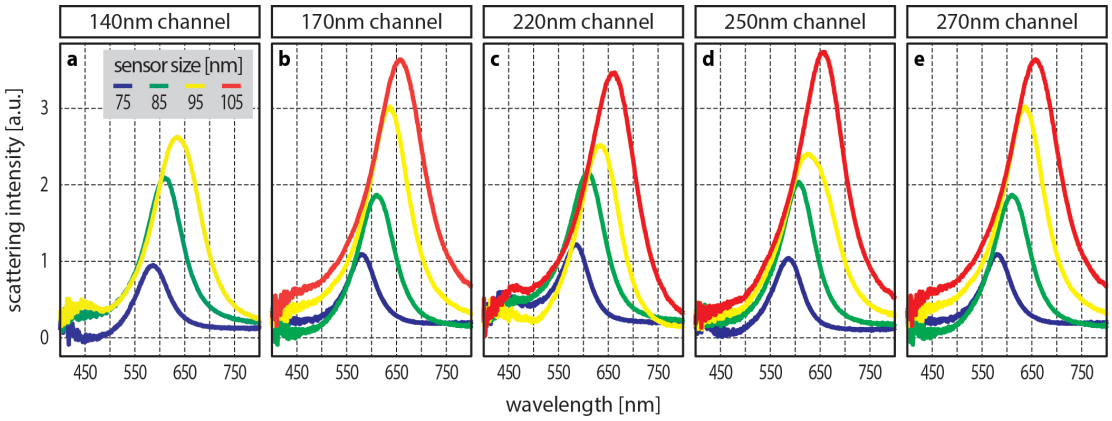

Figure S5. *Examples of scattering spectra of individual nanoantennas with different diameters (140 nm (a), 170 nm (b), 220 nm (c), 250 nm (d), 270 nm (e)) inside water-filled nanochannels with different widths, underlying the data shown in Fig. 2b.*

6. Peak linewidth for all particles analyzed in Figure 2

Figure S6 shows full width at half maximum (FWHM)values for the scattering spectra of the nanoantennas analyzed in Figure 2, in particular used to calculate the values of the FoM displayed in Figure 2d. Data points and error bars indicate the mean values and standard deviations, respectively, derived from four measurements.

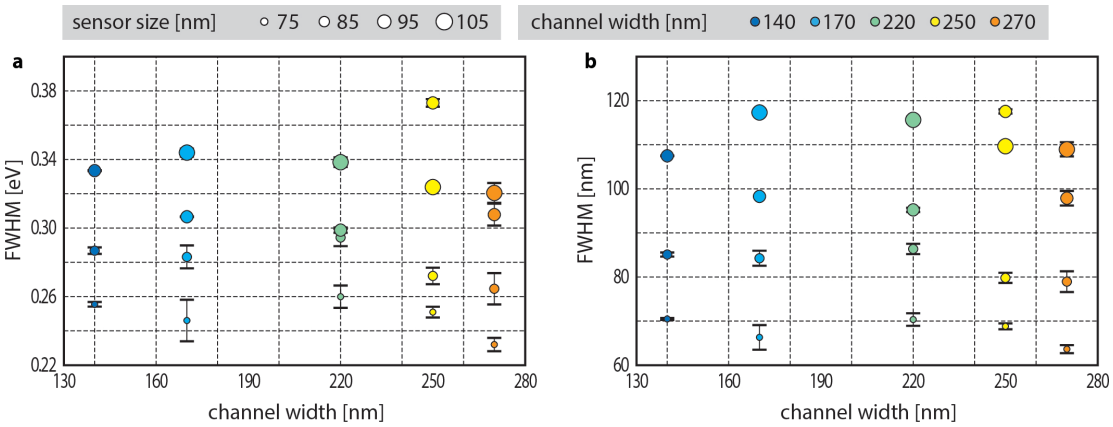

Figure S6. *The FWHM of the scattering spectra of the nanoantennas analyzed in Figure 4 both (a) in eV and (b) in nm. Note that some of the error bars are smaller than the used symbol and thus not visible.*

7. Experimental derivation of bulk refractive index sensitivity shown in Figure 2

Values of the bulk refractive index sensitivity (BRIS) shown in Figure 2c were determined as illustrated in Figure S7. For recording the scattering spectra of nanoantennas at different refractive indices of n_{water} = 1.33 and n_{glycol} = 1.44, the entire fluidic system was rinsed and filled with water and ethylene glycol, respectively. The LSPR λ_{water} and λ_{glycol} were found by fitting a polynomial of 2nd order to the 30 data points around the maximum of each scattering spectrum, and the sensitivity was calculated according to BRIS = $\Delta\lambda/(n_{glycol}-n_{water})$.

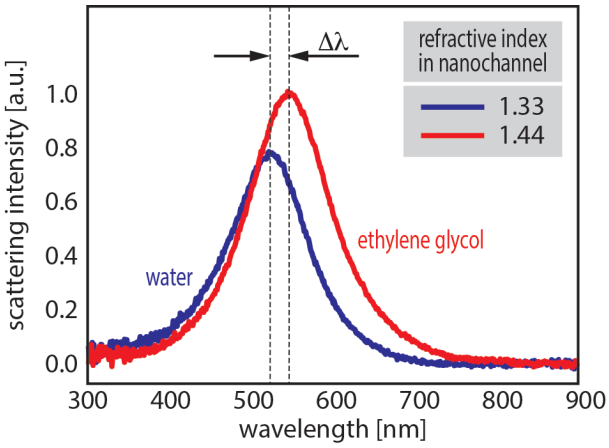

Figure S7. *Derivation of bulk refractive index sensitivity from experimental scattering spectra of a nanoantenna in water (blue) and in ethylene glycol (red). Two dashed lines indicate the LSPR peak shift* $\Delta\lambda$*, used for the calculation of the bulk refractive index sensitivity.*

8. Finite-Difference Time-Domain Simulations

To corroborate the experimental findings of the channel width dependence of the bulk refractive index sensitivity, we carried out FDTD simulations of a representative Au nanoantenna size (D= 80 nm) sandwiched inside a nanochannel with constant height (30 nm) and varying width, summarized in Figure S8a. As the main result, we find the same (observed in the experiments – Figure 2), basically linear, increase of the bulk refractive index sensitivity with channel width, once the gap between nanoantenna and channel walls is larger than the field decay length defined as the distance from the nanoantenna surface at which the field intensity has decayed to 1/e of its surface value. In the present case, the decay length is on the order of 25 nm, which is the lower limit of the gap between channel walls and Au nanoantenna used in our experiment. Mechanistically, the channel-width dependence of the bulk refractive index sensitivity can thus indeed be understood as a consequence of a smaller fraction of the sensing volume being occupied by the nanochannel walls, as the channel width increases, as quantitatively illustrated in the near-field plots in Figure S8b.

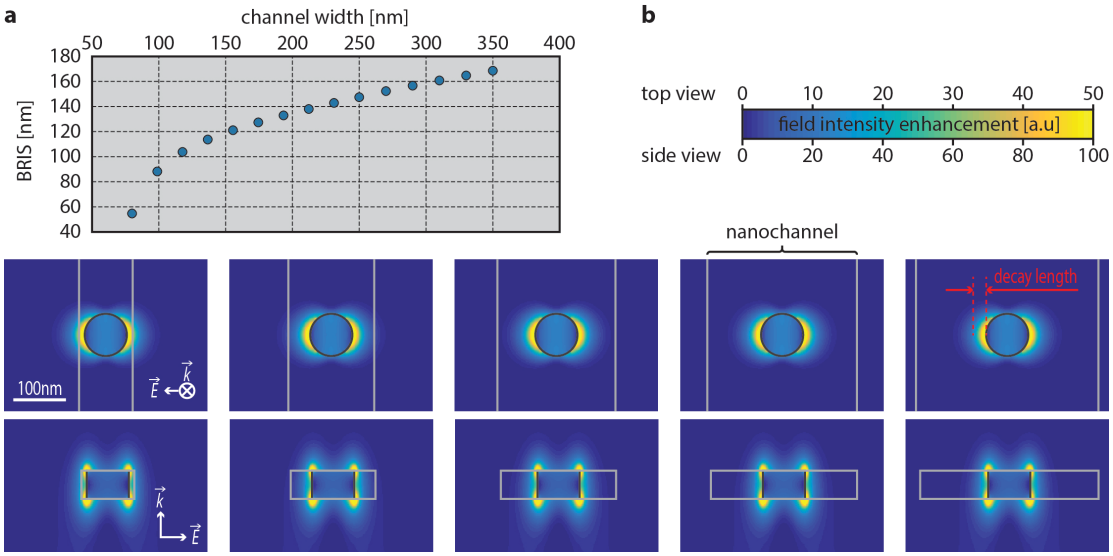

Figure S8. *Finite-Difference Time-Domain (FDTD) simulations. (a) Bulk refractive index sensitivity (BRIS) calculated by FDTD for an 80 nm Au disk nanoantenna sandwiched inside a 30nm high nanochannel with varying width. Note the linear dependence of the sensitivity in the regime, where gap between nanoantenna surface and nanochannel walls is larger than the field decay length defined as its intensity having decayed to 1/e of its surface value. In this regime, the FDTD results correlate well with the corresponding experimental data shown in Figure 3b. (b) Corresponding field intensity enhancement plots for different channel dimensions. The red line indicates the field decay length.*

9. Calibration of nanoplasmonic sensors for the analysis presented in Figure 4

Prior to monitoring the concentration c of a specific reagent, the used plasmonic antennas were calibrated by measuring their LSPR spectral peak positions λ_{max} and λ_{min} for both the highest and lowest involved concentration c_{max} and c_{min}, respectively, and linearly interpolating between the two values:

$$\lambda(c) = \frac{\lambda_{max}-\lambda_{min}}{c_{max}-c_{min}}(c - c_{min}) + \lambda_{min}.$$

In order to determine experimentally λ_{max} and λ_{min}, one microchannel was filled with the considered reagent fluid at concentrations c_{max}, while the other microchannel was filled with the considered reagent fluid at concentrations c_{min}. After that, λ was measured for a number of static differences in pressure, Δp, applied between the two microchannels. An example of the corresponding pressure-dependent LSPR peak position, $\lambda(\Delta p)$, of a plasmonic nanoantenna inside a nanochannel is shown in **Figure S9** for the case of c_{min} = 0 % and c_{max} = 60 % ethylene glycol in water. Clearly, the observed peak shift saturates at high values of $|\Delta p|$, indicating that the induced flow through the nanochannel is high enough to counteract diffusion, and that the local concentration c at the considered plasmonic sensor is the same as the concentration inside the microchannel at the higher pressure (*i.e.* $c = c_{max}$ or $c = c_{min}$). Therefore, the observed LSPR peak positions at high $|\Delta p|$ must be the sought values λ_{max} and λ_{min}.

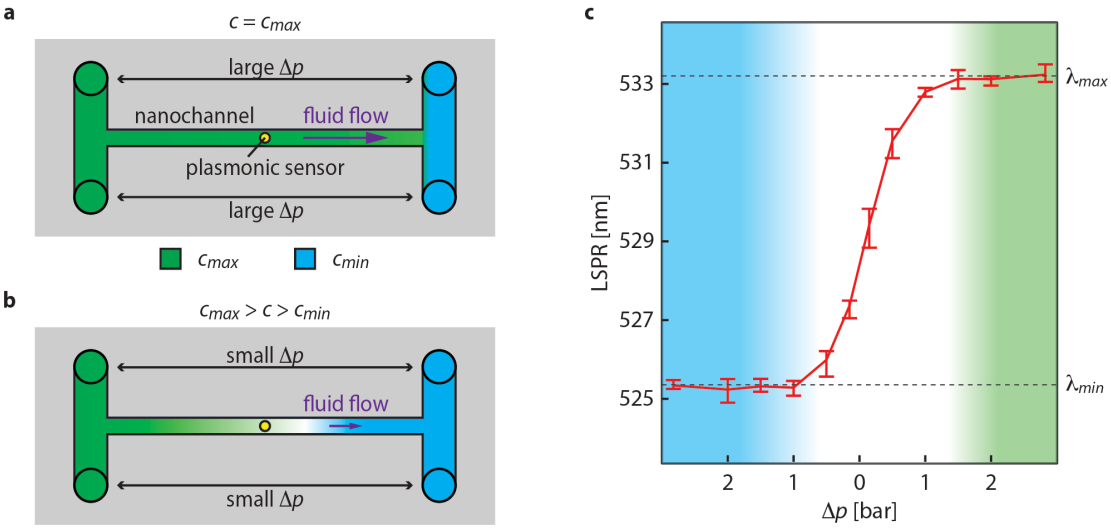

Figure S9 *Calibration of a nanoplasmonic sensor in a nanochannel. (a, b) Schematics illustrating the setup used to calibrate the nanoplasmonic sensor used for monitoring concentration of reagents. Left and right microchannels are filled with a considered reagent at concentration c_{max} and c_{min}, respectively, and a pressure difference Δp is applied*

between the two microchannels. (a) If $|\Delta p|$ *is sufficiently large, the local concentration c at the sensor to be calibrated is equal to the concentration in the corresponding microchannel. (b) For smaller values of* $|\Delta p|$*, diffusion is not entirely suppressed by the flow through the nanochannel, and* $c_{max} > c > c_{min}$*. (c) Measured LSPR of a nanoplasmonic sensor in a nanochannel as a function of pressure difference* $|\Delta p|$*, for the example of* c_{min} *= 0 % and* c_{max} *= 60 % ethylene glycol in water. Error bars indicate absolute deviations from mean values of 25 consecutive measurements. Colored and white backgrounds indicate regions of* $|\Delta p|$ *corresponding to the situations sketched in (a) and (b), respectively.*

10 . Spectral noise in peak shift and monochromatic readout schemes

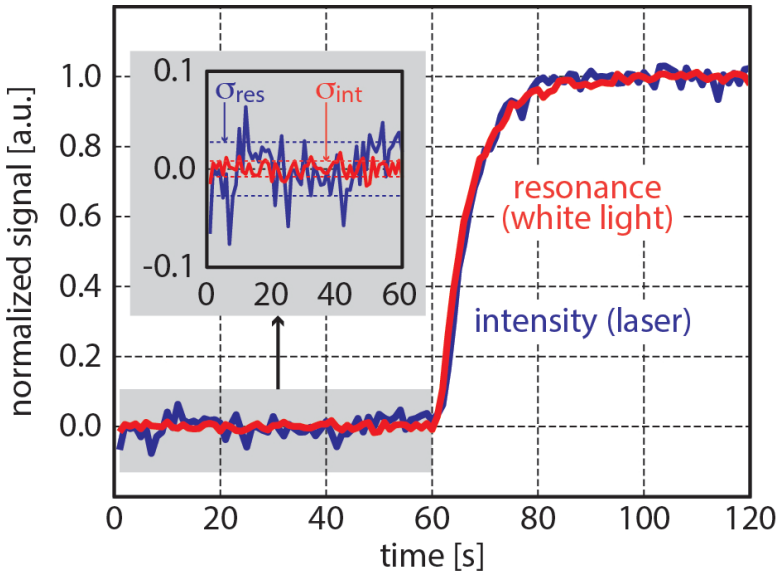

Figure S10 *Derivation of the spectral noise, σ, for traditional peak shift ("resonance") and monochromatic ("intensity") readout schemes for 1 s integration time in both cases. The measurement corresponds to a fluid exchange in the nanochannel from water to a water-ethylene glycol mixture. We find that* σ_{res} *= 0.027 and that* σ_{int} *= 0.008, implying a 3.5 times lower detection limit when using the monochromatic readout.*